ACS OMEGA

http://pubs.acs.org/journal/acsodf

Article

Effects of Tellurium Doping on Environmental Stability and Luminous Performance of $CsPbBr_3$ Quantum Dots

Zhenyao Liang, Liang Ni, Yang Zhang, Chen Yuan, Le Huang, Yibin Yang, and Ye Xiao*

Cite This: *ACS Omega* 2022, 7, 21800−21807

Read Online

ACCESS | Metrics & More | Article Recommendations | Supporting Information

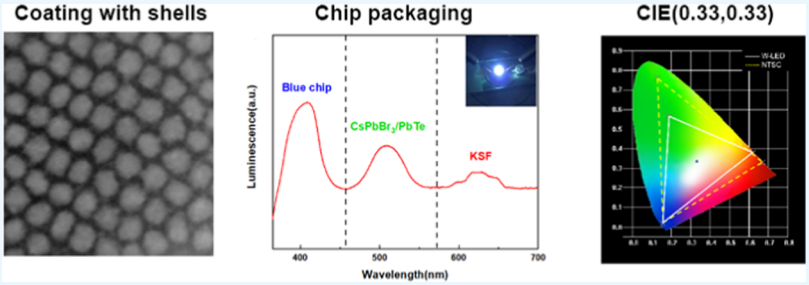

ABSTRACT: The effects of elemental tellurium doping and decorating on the photoluminescence quantum yield (PL QY) and the environmental stability of the $CsPbBr_3$ quantum dots (QDs) have been systematically studied. The PL spectra blue-shifts from 520 to 464 nm gradually with the increase in the amount of Te, and the full width at half-maximum (FWHM) increases from 20 to 62 nm and decreases to 27 nm accordingly. The morphology of the untreated samples has a rectangular shape with distinct boundaries, whereas the Te-doped samples have a semi-core−shell structure with partially coated $CsPb_2Br_5$ after tellurium doping. Furthermore, the apparent size of the nanocomposites increases to 20 nm, but the crystal size of the core decreases slightly according to the broadened peaks of X-ray diffraction (XRD). Further investigation by X-ray photoelectron spectroscopy shows that the binding energy of Pb−Br increases and Pb−Te bonds are formed in Te-doped samples, which can enhance the stability of QDs from the view of strengthening the chemical bonds and inhibiting the detaching behavior of bromine under moisture. At the nominal content of Pb/Te = 1:0.4, the thermal decomposition temperature of the QDs increases from 300 to 500 °C; the maximum of PL QY increases to 70% for the 1:0.4 sample and the relative PL peak intensity maintains 50% of the initial value after a 60 h aging simulation. Finally, the nanocomposite materials are fabricated into a white light-emitting device (WLED). Under the illumination of a commercial GaN chip, the device shows a good Commission Internationale de lEclairage (CIE) color coordination of (0.3291,0.3318).

INTRODUCTION

Stimulated by the benefits of low-cost, brightness, and easily tunable emission spectral for the all-inorganic lead halide perovskites (IOHP) based quantum dots (QDs),[1] much effort has been made continuously for applications on optoelectronic devices,[2] such as light-emitting diodes (LED),[3] photodetectors,[4] laser diodes,[5] etc. In the scenario of all-white-LED chips, the gamut of red, green, and blue require good color purity and brightness. However, owing to the intrinsic ionic nature of the bonds of $CsPbX_3$,[6] the soft lattices result in a lower small formation energy of vacancies and an enormous concentration of halide vacancies;[7] furthermore, the detaching of ligand in the moisture is more severe,[8] those combined effects would deteriorate the brightness of QDs and gradually quench the PL intensities. To tackle the above shortcomings, various kinds of attempts have been made to enhance the stability against moisture, polar solvents, and ultraviolet. Among those efforts, doping may increase the Pb−X bond strength and increase the formation energy of vacancies;[9] therefore, related studies on Sn,[10] Zn,[11] Co,[12] and Mn[13] as doping agents have been continuously reported previously. It is known that the coating of IOHP QDs into a shell composed of silica,[14] macromolecules, and other inorganic semiconductors,[15] is a good method to prevent the penetration of oxygen and moisture. Interestingly, interface modifications can also be realized as the accompanying surface doping and possible shells on the QDs could be in situ formed at the same time.[16] Combined with the above considerations, elemental Te is chosen as the doping agent. By increasing the nominal Te content, the crystalline of QDs has been distorted to a tetragonal phase from the initial cubic phase gradually. As a consequence, the PL peak blue-shifts gradually and transforms

Received: March 30, 2022
Accepted: June 3, 2022
Published: June 15, 2022

https://doi.org/10.1021/acsomega.2c01891
ACS Omega 2022, 7, 21800−21807

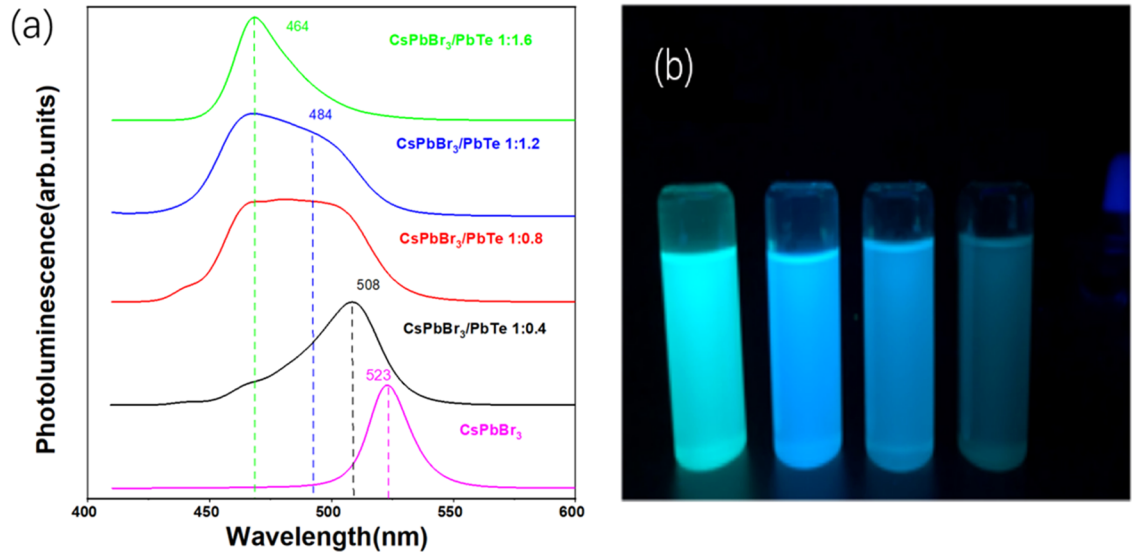

Figure 1. (a) Photoluminescence spectra for samples. (b) Color of samples with different ratios of Pb/Te under 365 nm UV light. ("Photograph courtesy of "Liang Ni." Copyright 2022." The photo is in the free domain).

from unimodal distribution, to bimodal distribution, and finally to unimodal distribution around 464 nm after a higher Te content. As evident from the XPS analysis, the binding energy of Pb−Br increases due to the addition of Te, which increases the thermal stability. Finally, after optimizing the emission spectrum and a modulated nominal content, the 0.4% QD-based white-LED device has a CIE color coordination of (0.31,035), which is closer to the idealized coordination of (0.33,0.33).[17]

EXPERIMENTAL PROCEDURES

The raw materials, cesium carbonate (99.9%), lead bromide (99.9%), tellurium powder (99.9%), oleic acid (90%), oleylamine (80−90%), 1-octadecene (90%), tri-n-octylphosphine (90%), 1-dodecanethiol (99.9%), *n*-hexane (99.9%), 2-butanol (99.9%), and toluene (99%), were all from Aladdin Reagent and used without any purification.

The preparation procedures for cesium oleate were as follows: 0.2602 g of cesium carbonate, 1 mL of oleic acid, and 15 mL of 1-octadecene were added to a 100 mL three-necked flask and then heated to 150 °C under nitrogen protection atmosphere until all cesium carbonate in the solution dissolved in the solvent.

The preparation procedures for lead bromide were as follows: 0.1468 g of lead bromide, 1 mL of oleic acid, 1 mL of oleylamine, and 10 mL of 1-octadecene were added to a 100 mL three-necked flask and then heated to 180 °C under nitrogen protection atmosphere until all lead bromide in the solution dissolved in the solvent.

The preparation of $CsPbBr_3$ QDs solutions was as follows: the precursor solution of lead bromide was kept at 180 °C for 1 h and 0.8 mL of cesium oleate solution was injected into it. After heating and stirring for 30 s, the flask was quickly cooled to room temperature in an ice-water bath. Then, the reaction solution was centrifuged at 10 000 rpm for 8 min. The supernatant was discarded and the pellet was collected. The pellet was redissolved in 4 mL of toluene, and the centrifugation operation was repeated. The resulting precipitate was dissolved in 5 mL of toluene solution for further use.

The preparation procedures for Te were as follows: 10, 20, 30, and 40 mg of tellurium powder were respectively added to a 10 mL sample bottle with 1 mL of tri-n-octylphosphine, 1 mL of 1-dodecanethiol, and 2 mL of 1-octadecene. Then, the mixture was shaken ultrasonically for 5 min to dissolve the tellurium powder. The mixed solution was stirred and heated at 120 °C until the powder was completely dissolved. The pale yellow transparent solution was used in the next step.

The preparation of the Te-doped $CsPbBr_3$ solution was as follows: the prepared $CsPbBr_3$ quantum dot solution was heated at 180 °C for 15 min, and 0.5 mL of precursor solutions with different contents of tellurium was injected into it. The mixture was heated to 190 °C for 30 min under magnetic stirring and centrifuged at 10 000 rpm for 8 min after it turned dark green. The supernatant was discarded and the pellet collected. The pellet was redissolved in 2 mL of toluene and 2 mL of 2-butanol by sonication. The centrifugation operation was repeated. The resulting precipitate was dissolved in 5 mL of toluene solution for further characterization.

The PL QY measurements were conducted in a 6 in. photometric integrating sphere through the Fluorolog-3 (HORIBA), and the data error was less than 1%.

CHARACTERIZATION DETAILS

The transmission electron microscopy and high-resolution transmission electron microscopy (HRTEM) were performed by Talos F200S (Thermo. Inc.). The X-ray diffraction patterns were recorded by D8 ADVANCE(Bruker) using Cu Kα radiation (1.54Å). The fluorescence spectra were measured using a Fluorolog-3 spectrophotometer and Shimadzu Ultraviolet-2100 (HORIBA). The energy-dispersive spectra were collected by Escalab 250Xi (Thermo Fisher). Thermogravimetry was measured by TGA/DSC3+ Nicolet IS50 (Mettler Toledo).

RESULTS AND DISCUSSION

As the content of the additional elemental Te is normalized in the ratio of Pb, for better clarification, the samples are labeled as $CsPbBr_3$/PbTe 1:*x*, whereas the *x* is the nominal content, which varies from 0 to 1.6. The photoluminescence spectra of

https://doi.org/10.1021/acsomega.2c01891
ACS Omega 2022, 7, 21800−21807

different nominal content of Te were studied under a 395 nm blue light source. As shown in Figure 1a, the initial PL peak of untreated undoped $CsPbBr_3$ is around 523 nm. The PL blue-shifts to a lower wavelength with the increase in the nominal content of Te, which is consistent with the faded colors in Figure 1b. The UV−vis spectra in Figure S1 indicate an increased band gap from 2.37 eV (523 nm) to 2.9 eV (427 nm). Apparently, it does not correlate with the PL peaks around 464 nm for the x = 1.6 sample, which means that the PL peaks for samples with a high Te content are not merely composed of the band edge transition or exciton emissions. The absorption bands on the 398 nm should be attributed to $PbBr_2$.[18] Furthermore, the FWHM of samples are 20, 34, 62, 56, and 27 nm, with the mark x varying from 0 to 1.6, respectively. The broadened peaks may be attributed to different combined mechanisms; first, the increased size distribution[19,20] as the quantum confinement effect, which slightly increases the FWHM from the standard exciton emission, and second, different radiative recombination channels induced by possible energy states, which would largely increase the FWHM to 62 nm. However, the decreasing trend of the FWHM after x = 0.8 is discussed together with the phase structure studies later.

Apparently, such severe variations in PL peak mean that the crystal structures have changed, which could be clearly observed in the XRD patterns. As it is known that the crystal structures of perovskites are quite sensitive to the tilting of $[PbBr_6]^{4-}$ octahedron cages,[21] doping on the Br sites with tellurium alters the length and strength of Pb−X bonds; therefore, the octahedron cages tilted and decreased the degree of crystallography symmetry. Thus, the cubic phase gradually degenerates as the agent Te induces the excess of free Br^-, thereby forming a $PbBr_2$-rich condition as evidenced in the UV−vis spectra (398 nm absorption band in Figure S1). The equation of $CsPbBr_3 + PbBr_2 \rightarrow CsPb_2Br_5$ is then balanced.[22] As seen in Figure 2, the crystal phase of the control group can be indexed to standard JCPDF #054-0752 quite well. After doping, the intensities of the major peaks of the cubic phase decreases. The (021) plane for PbTe at 26.550° and the (002) plane for $CsPb_2Br_5$ at 11.738° can be observed for the x = 0.8 sample. Further increase in the content of Te increases the (002) peaks of $CsPb_2Br_5$, which can be seen in Figure S2, indicating that the volume fraction of the indirect band gap phase, i.e., $CsPb_2Br_5$ increases after doping with large amount of Te. It is reported that the $CsPb_2Br_5$ phase has an indirect band gap; therefore, the brightness would be decreased with the decrease in the efficiency of indirect optical transitions, which is consistent with the gradually faded colors in Figure 1b.

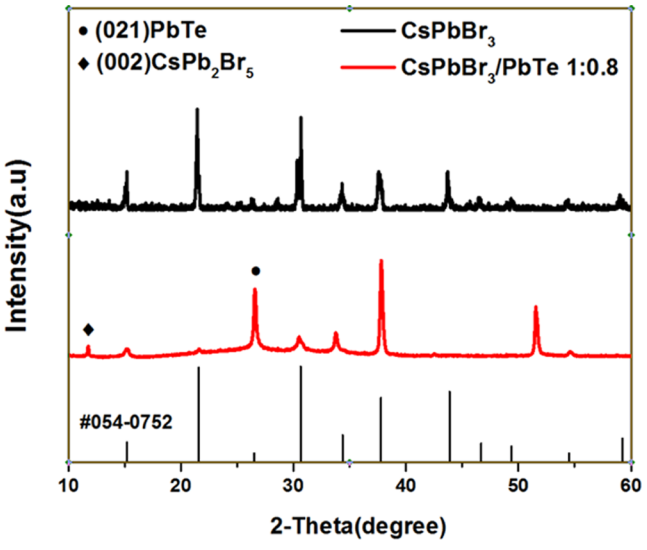

Figure 2. XRD patterns of undoped and $CsPbBr_3$/PbTe 1:0.8 samples.

The morphologies of the doped and undoped samples is shown in Figure 3a,c, and their distribution histograms are shown in Figure 3b,d respectively. First, the control samples have a morphology of rectangles with sharp edges, while the $CsPbBr_3$/PbTe 1:0.8 samples have a core−shell microstructure with fuzzy boundaries. We speculate that the second phase $CsPb_2Br_5$ forms shells around the QDs as evidenced in earlier reports.[18,23] The majority size of control samples is about 9−16 nm, which is lower than that of $CsPbBr_3$/PbTe 1:0.8 (15−22 m). However, the enlarged full width at half-maximum of the main XRD diffraction peaks indicates a shrinkage of the crystal size, that is to say, the size of the core−shell composites increases but the core of QDs decreases, which leads to a blue shift of the PL peaks as the actual size of the luminous cores decreases. Furthermore, the size distributions become wider after tellurium doping, which can be the reason for the slight increase in FWHM from 20 to 34 nm for the x = 0.4 sample. As the content of Te doping increases, the crystal defects induced by trace-transformed $CsPb_2Br_5$ introduce related defect states, and the energy transfer from different energy states also contributes to different PL emissions with different peak centers. For the x=1.6 sample, the increasing degree coating $CsPbBr_3$ by $CsPb_2Br_5$ increases the overlap of wavefunctions of the electrons and holes and thus decreases the FWHM for enhanced radiative quantum transition rate.[23] Unfortunately, because $CsPb_2Br_5$ has an indirect band gap, the intensity of PL emission decreases by several magnitudes and thus can not be observed by bare eyes under UV light illumination.

To further study the microstructure of the core−shell composites, HRTEM microscopy was conducted. As seen in Figure 4a,b, the control sample has distinct boundaries with a 4.03 Å interplanar spacing, which can be ascribed to the second strong absorption peak for the (110) planes of cubic $CsPbBr_3$. After Te doping, the signal of QDs becomes fuzzy, resulting in a 3.36 Å interplanar spacing in Figure 4d, which can be ascribed to the (021) plane of PbTe. It is note worthy that the PbTe phase is in an isolated state, which is hard to clean out in the solution. The boundaries of PbTe are not coherent with the perovskite phases, but the band gap of PbTe is too small to introduce significant PL emissions around visible light. In this case, $CsPb_2Br_5$ forms shells that partially cover the core of QDs, as the solid reaction of $PbBr_2$ + $CsPbBr_3$ = $CsPb_2Br_5$ is inadequate. The EDS energy mapping results in Figure S3a−c show the uniformly dispersed Cs, Pb, and Br on the QDS, respectively. Of note, the tellurium is introduced in a liquid state, and the enrichment of the signals from Te elements surrounding the perovskite cores can be distinguished in the dashed circles in Figure S3d.

To analyze the chemical bond environment after Te doping, XPS spectroscopy was conducted for the $CsPbBr_3$/PbTe 1:0.8 samples. All elements were calibrated with C 1s, and the C 1s and O 1s spectra can be observed in Figure S4a,b, respectively. As presented in Figure 5a, the Cs $3d_{5/2}$ and $3d_{3/2}$ peaks hardly

https://doi.org/10.1021/acsomega.2c01891
ACS Omega 2022, 7, 21800−21807

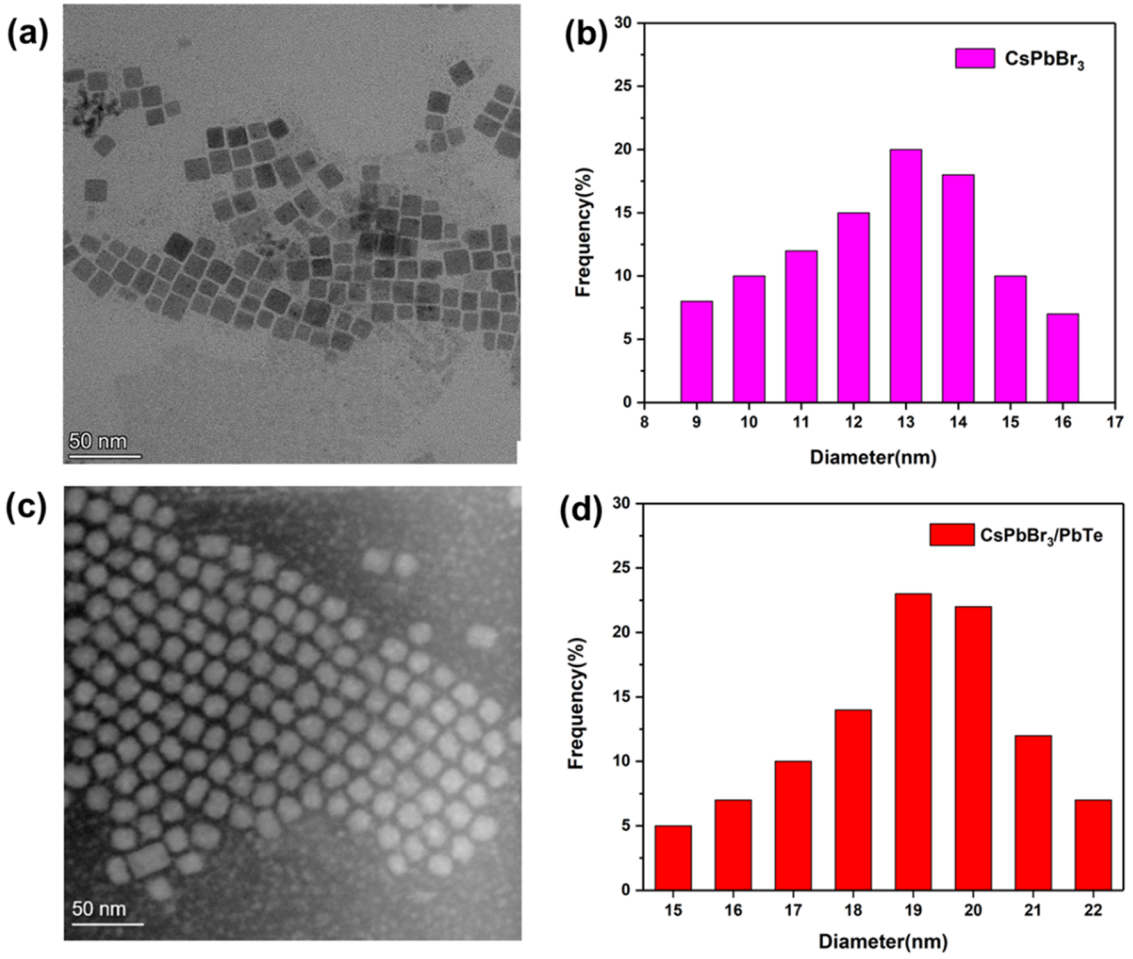

Figure 3. (a) TEM image of the control samples. (b) Particle size distribution histogram of the control samples. (c) TEM image of $CsPbBr_3$/PbTe 1:0.8 samples. (d) Particle size distribution histogram for the $CsPbBr_3$/PbTe 1:0.8 samples.

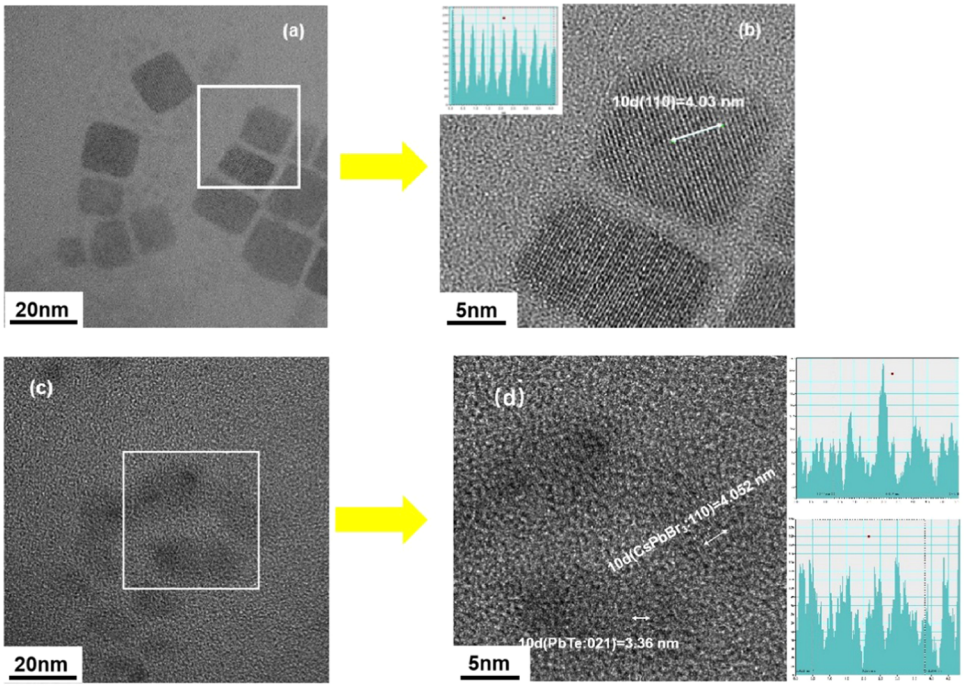

Figure 4. (a) TEM image of the individual control sample. (b) HRTEM image and *d*-spacing histogram for (a). (c) TEM image of the individual $CsPbBr_3$/PbTe 1:0.8 sample. (d) HRTEM image and *d*-spacing histogram for (c).

https://doi.org/10.1021/acsomega.2c01891
ACS Omega 2022, 7, 21800−21807

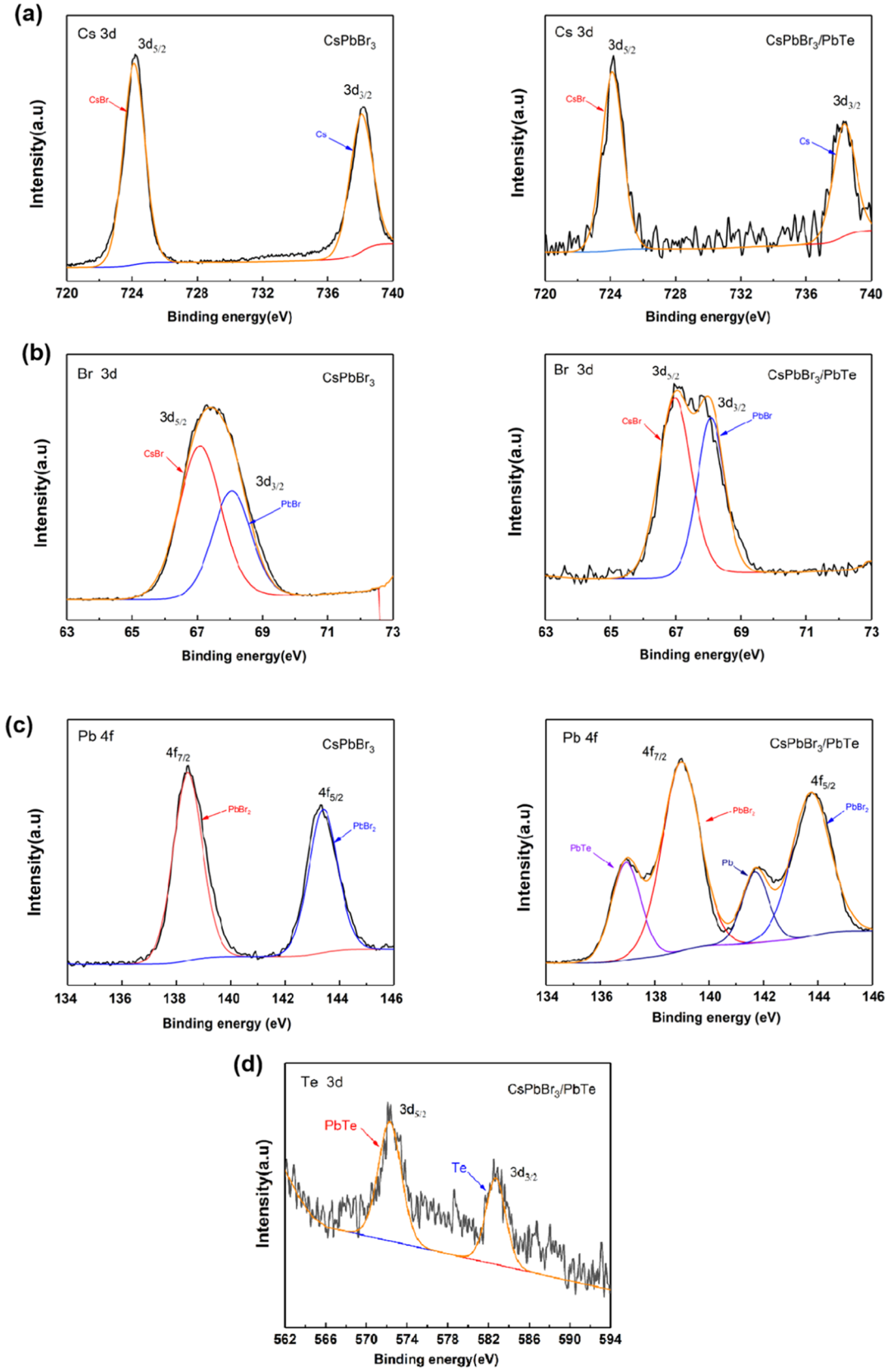

Figure 5. Comparisons of XPS spectra for Cs 3d (a), Br 3d (b), Pb 4f (c), and Te 3d (d) of $CsPbBr_3$/PbTe 1:0.8 samples.

changed after tellurium doping as Cs contributes little to the electronic structures. Similarly, the peaks in Figure 5b for Br $3d_{5/2}$ and $3d_{3/2}$ are located at 67.1 and 68.2 eV despite tellurium doping, indicating that the limited solubility of tellurium atoms in the lattice has little effect on the chemical environment around Br ions. In contrast, the Pb $4f_{7/2}$ and $4f_{5/2}$ peaks in Figure 5c shift to higher energy, which increases from 138.3 to 138.9 eV. Moreover, the binding energy peak around

https://doi.org/10.1021/acsomega.2c01891
ACS Omega 2022, 7, 21800−21807

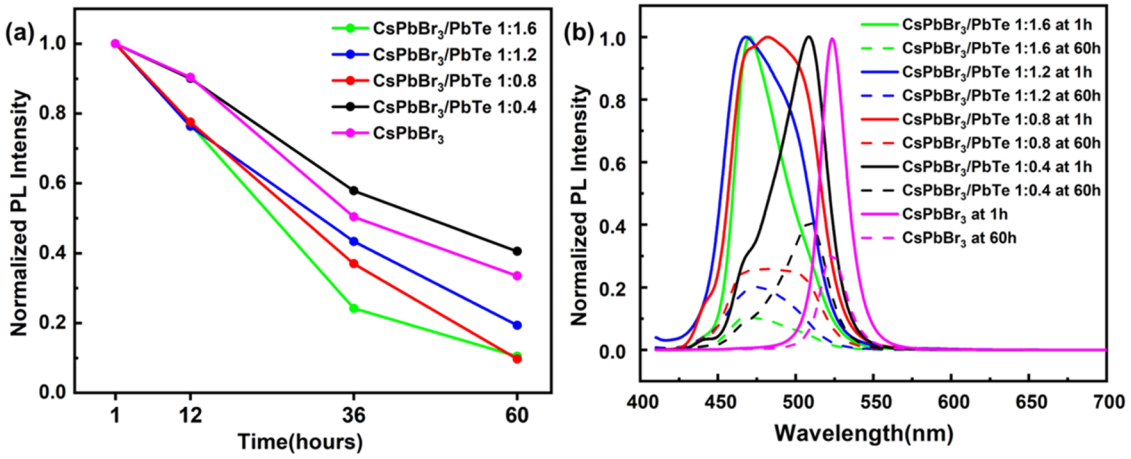

Figure 6. Investigations for photoluminescence stabilities of materials in hexane solution stored under ambient air compared those stored for 1, 12, 36, and 60 h: (a) normalized PL intensities for control and composite perovskites and (b) normalized photoluminescence spectra.

136.9 eV for the Pb−Te bond can be observed in Figure 3c. Combined with the spectra of Te $3d_{5/2}$ and $3d_{3/2}$ in Figure 5d, the binding energy elementary tellurium around 583 eV is also captured. Therefore, it can be concluded that the Te atoms are actually doped into the Br sites and form Pb−Te bonds, and the nominal content of 1:0.8 exceeded the solubility of tellurium in $CsPbBr_3$ and then precipitated as PbTe. However, it is difficult to exclude the existence of elementary tellurium and PbTe in the solvent, and a peak around 583 eV is the origin of the dispersed signals in EDS mapping (Figure S2). As the binding energy of Pb−Br increased, the stability of $CsPbBr_3$ increased accordingly.[24] Therefore, the thermal stability measurements were conducted by TGA as the shell of $CsPb_2Br_5$ increases the structural stability. As shown in Figure S5a, there are two decomposition temperatures for the initial $CsPbBr_3$ samples, which are 300 and 600 °C; after optimizing the doping content of Te, the numbers in Figure S3b increases to 500 and 700 °C, respectively.

The accelerated aging simulations have been conducted as follows: the samples were exposed to ambient air after redissolving in the hexane solution, and the PL spectra were measured at different durations. As presented in Figure 6a, the normalized PL intensities with their initial intensities decreased as the time elapsed; however, among those samples, $CsPbBr_3$/PbTe 1:0.4 QDs showed the highest percentages; further increase in the nominal content of Te decreases the PL intensities, which means that the high doping content introduces unfavorable defects from the view of PL properties. In Figure 6b, the FWHM for PL peaks after 60 h aging for $CsPbBr_3$/PbTe 1:0.4 increases less than that in other samples. A moderate doping content in QDs has the ability to inhibit the detachment of halogen atoms to some degree. Note worthy, the simulation condition of dispersion in solvents is much harsher than that in conventional situations, which are subjected to electronic packaging and exposed to an ambient environment; therefore, the relatively increased stability of $CsPbBr_3$/PbTe 1:0.4 after 60 h indicates that the failure probability is reduced to a considerable extent.

To study the PL dynamics of the doping content on the QDs, time-resolved PL decay curves are measured. As presented in Figure 7, the curves have a typical shape of biexponential exponent functions, which can be expressed as $I(t) = A_1 \exp(-t/\tau_1) + A_2 \exp(-t/\tau_2)$, τ_1 and τ_2 are the average lifetimes of different decay pathways, respectively, and

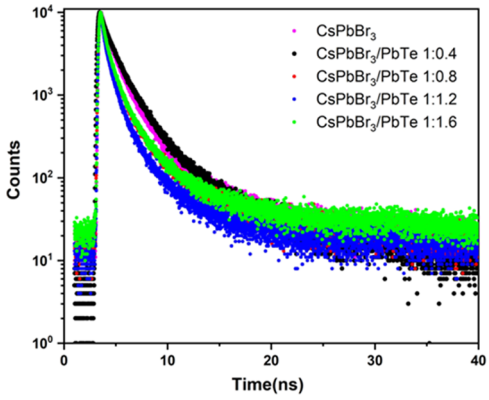

Figure 7. PL decay of perovskite different content of tellurium.

A_1 and A_2 are the corresponding weight ratios. By measuring the PL QY and exacting the weight of radiative combination rate k_r and nonradiative combination rate k_{nr} by the equation of PL QY = $k_r/(k_r + k_{nr})$, combined with the equation of $\tau_{avg} = 1/(k_r + k_{nr})$, the parameters can be solved.[25] As presented in Table 1, the PL QY increases slightly to 70% at a lower content of Te and decreases with the increasing content of Te. As the radiative combination rates show only marginal changes, which fluctuate around 8.57 to 13.12 × 10^7 s^{-1}, the major cause of the variational PL QY is the several-fold changes in the nonradiative combination rate from 4.07 to 23.17 × 10^7 s^{-1}. For the lower content of Te, a 30% decrease in k_{nr} benefits the PL intensity. The fact that a proper content of Te doping could decrease the possibility of nonradiative recombination relies on the increased bond strength of Pb−Br as partially Te doping

Table 1. PL Decay Kinetic Parameters for Different Te Nominal Contents

sample	τ_1 (ns)	τ_2 (ns)	τ_{avg} (ns)	PL QY (%)	k_r (10^7 S^{-1})	k_{nr} (10^7 S^{-1})
$CsPbBr_3$	4.47	15.56	6.15	62	10.08	6.18
Pb/Te = 1:0.4	5.50	16.40	7.36	70	9.51	4.07
Pb/Te = 1:0.8	5.20	13.62	4.19	55	13.12	10.73
Pb/Te = 1:1.2	2.23	10.41	3.21	35	10.89	20.22
Pb/Te = 1:1.6	2.931	12.81	3.15	27	8.57	23.17

https://doi.org/10.1021/acsomega.2c01891
ACS Omega 2022, 7, 21800−21807

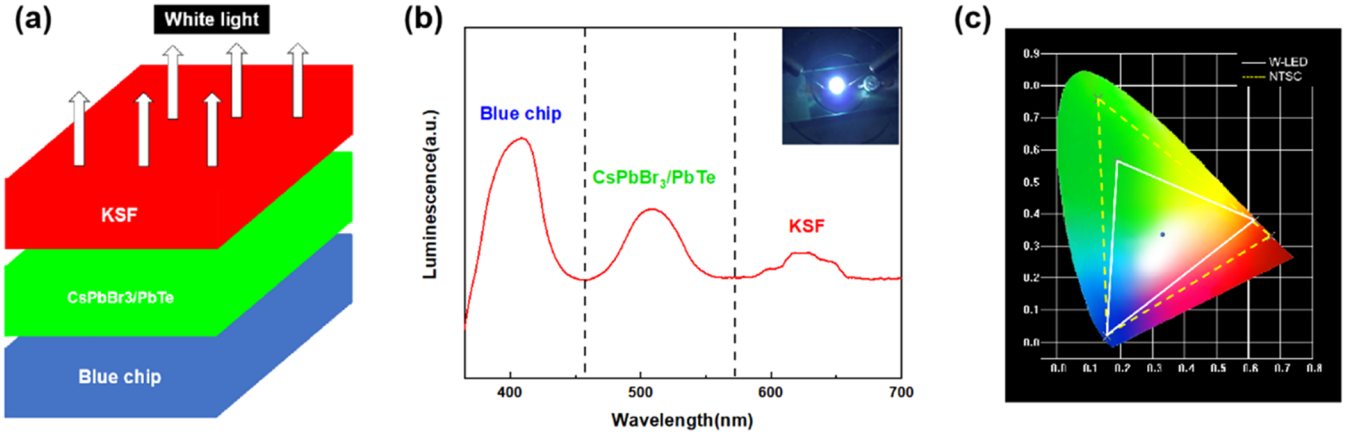

Figure 8. (a) Schematic diagram of a white LED. (b) Electroluminescence spectrum under current excitation. The inset figure is the digital image. (c) CIE color coordinates of the white LED.

and surface decorating, thus the possibility of detaching for surface atoms has decreased, which is evidenced in the XPS spectra. However, further increasing the nominal content of Te introduces more surface defect states, which are usually deep-level states; therefore, the high content of Te is not favorable for further applications from the points of view of both environmental inertia and PL specialties of perovskites.

Therefore, as $CsPbBr_3$/PbTe 1:0.4 QDs have the best stability, the slightly doped samples are chosen as the green luminescent layer in the white-LED chips. The schematic diagram of the white-LED chip is shown in Figure 8a. As seen in the EL spectrum in Figure 8b, the spectrum has a combination of emission peaks from the blue emission of GaN chip, the green emission of Te-doped $CsPbBr_3$ QDs, which is consistent with the PL spectra, and the red emission of commercial KSF. The slightly broadened green gamut has few side effects on the composed white color. The optimized ratio of the luminescent materials, an all-white-LED device with a CIE color coordination (0.3291,0.3318), is obtained with enhanced stability. The color index is comparable with the standard white color coordination (0.33,0.33), and the gamut area index is 30% larger than the NTSC standard.

CONCLUSIONS

The Te-doped $CsPbBr_3$ quantum dots have been fabricated using the thermal injection method. The photoluminescence quantum yield (PL QY) and the environmental stability of the $CsPbBr_3$ quantum dots (QDs) have been improved through elemental tellurium doping and surface decorating strategies. The position of the excitation peak gradually shifts to higher wavelengths with the increasing amount of Te. The peak width first increases at a lower doping content and then gradually decreases, which is induced by the size effects combined with energy transfers in defect states. The QDs transform to a tetragonal phase. In comparison with the untreated samples, the QDs have a morphology of squares with distinct boundaries. The morphology of the composites appears in a core−shell structure with fuzzy boundaries after doping and surface decoration. The XPS analysis proves that the binding energy of Pb−Br increases and Pb−Te bonds are formed after doping. From the view of increased chemical bond strength, the stability of QDs is increased, and the loss of bromine is inhibited accordingly. At the nominal content of 0.4 atom %, the upper limits of the temperature tolerance of the QDs increased to 200 °C; the relative PL intensity maintains 50% of the initial intensity after a 60 h simulated accelerated aging test. Overall, the composite materials are fabricated into white light-emitting devices (WLEDs). Under the illumination of a commercial GaN chip and commercial KSF powders, the device shows a good CIE color coordination of (0.3291,0.3318).

ASSOCIATED CONTENT

Supporting Information

The Supporting Information is available free of charge at https://pubs.acs.org/doi/10.1021/acsomega.2c01891.

UV−vis spectra (Figure S1), the enlarged XRD spectra (Figure S2), EDS mapping images for undoped (Figure S3), XPS spectra for C 1s and O 1s (Figure S4), and TGA measurements for elemental distribution (Figure S5) (PDF)

AUTHOR INFORMATION

Corresponding Author

Ye Xiao − *School of Materials and Energy, Guangdong University of Technology, Guangzhou 510006, China;* orcid.org/0000-0001-5813-8430; Email: yexiao@gdut.edu.cn

Authors

Zhenyao Liang − *School of Materials and Energy, Guangdong University of Technology, Guangzhou 510006, China*

Liang Ni − *School of Materials and Energy, Guangdong University of Technology, Guangzhou 510006, China*

Yang Zhang − *School of Materials and Energy, Guangdong University of Technology, Guangzhou 510006, China*

Chen Yuan − *School of Materials and Energy, Guangdong University of Technology, Guangzhou 510006, China*

Le Huang − *School of Materials and Energy, Guangdong University of Technology, Guangzhou 510006, China;* orcid.org/0000-0003-3189-2171

Yibin Yang − *School of Materials and Energy, Guangdong University of Technology, Guangzhou 510006, China;* orcid.org/0000-0003-4845-4530

Complete contact information is available at: https://pubs.acs.org/10.1021/acsomega.2c01891

https://doi.org/10.1021/acsomega.2c01891
ACS Omega 2022, 7, 21800−21807

Notes

The authors declare no competing financial interest.

■ ACKNOWLEDGMENTS

This work was supported by the National Natural Science Foundation of China (Grant No. 51602065).

■ REFERENCES

(1) Tang, F.; Su, Z. C.; Ye, H.; Zhu, Y.; Dai, J.; Xu, S. J. Anomalous variable-temperature photoluminescence of CsPbBr3 perovskite quantum dots embedded into an organic solid. *Nanoscale* **2019**, *11*, 20942−20948.

(2) Li, X.; Yu, D.; Cao, F.; Gu, Y.; Wei, Y.; Wu, Y.; Song, J.; Zeng, H. Healing All-Inorganic Perovskite Films via Recyclable Dissolution-Recyrstallization for Compact and Smooth Carrier Channels of Optoelectronic Devices with High Stability. *Adv. Funct. Mater.* **2016**, *26*, 5903−5912.

(3) Lin, H.; Mao, J.; Qin, M.; Song, Z.; Yin, W.; Lu, X.; Choy, W. C. H. Single-phase alkylammonium cesium lead iodide quasi-2D perovskites for color-tunable and spectrum-stable red LEDs. *Nanoscale* **2019**, *11*, 16907−16918.

(4) Xie, C.; Liu, C. K.; Loi, H. L.; Yan, F. Perovskite-Based Phototransistors and Hybrid Photodetectors. *Adv. Funct. Mater.* **2020**, *30*, No. 1903907.

(5) Zhang, C.; Duan, J.; Qin, F.; Xu, C.; Wang, W.; Dai, J. CsPbBr3 interconnected microwire structure: temperature-related photoluminescence properties and its lasing action. *J. Mater. Chem. C* **2019**, *7*, 10454−10459.

(6) Cao, D. H.; Guo, P.; Mannodi-Kanakkithodi, A.; Wiederrecht, G. P.; Gosztola, D. J.; Jeon, N.; Schaller, R. D.; Chan, M. K. Y.; Martinson, A. B. F. Charge Transfer Dynamics of Phase-Segregated Halide Perovskites: CH3NH3PbCl3 and CH3NH3PbI3 or (C4H9NH3)2(CH3NH3) n-1Pb nI3 n+1 Mixtures. *ACS Appl. Mater. Interfaces* **2019**, *11*, 9583−9593.

(7) Deng, J.; Li, J.; Yang, Z.; Wang, M. All-inorganic lead halide perovskites: a promising choice for photovoltaics and detectors. *J. Mater. Chem. C* **2019**, *7*, 12415−12440.

(8) Guo, X.; Gong, Q.; Borowiec, J.; Zhang, S.; Han, S.; Zhang, M.; Willis, M.; Kreouzis, T.; Yu, K. Energetics of Nonradiative Surface Trap States in Nanoparticles Monitored by Time-of-Flight Photoconduction Measurements on Nanoparticle−Polymer Blends. *ACS Appl. Mater. Interfaces* **2019**, *11*, 37184−37192.

(9) Parobek, D.; Dong, Y.; Qiao, T.; Son, D. H. Direct Hot-Injection Synthesis of Mn-Doped CsPbBr3 Nanocrystals. *Chem. Mater.* **2018**, *30*, 2939−2944.

(10) Abib, M. H.; Li, J.; Yang, H.; Wang, M.; Chen, T.; EnzeXu; Jiang, Y. Direct deposition of Sn-doped CsPbBr3 perovskite for efficient solar cell application. *RSC Adv.* **2021**, *11*, 3380−3389.

(11) Ding, L.; Liu, S.; Zhang, Z.; Shao, G.; Xiang, W.; Liang, X. Stable Zn-doped CsPbBr3 NCs glasses toward an enhanced optical performance for WLED. *Ceram. Int.* **2019**, *45*, 22699−22706.

(12) Wang, C.; Long, Y.; Liu, X.; Fu, S.; Wang, J.; Zhang, J.; Hu, Z.; Zhu, Y. A dual promotion strategy of interface modification and ion doping for efficient and stable carbon-based planar CsPbBr3 perovskite solar cells. *J. Mater. Chem. C* **2020**, *8*, 17211−17221.

(13) Song, L.; Huang, L.; Xiao, W.; Li, J. Role of octahedral deformation in the broad-band emission in Mn-doped lead halide perovskite: First-principles investigation for the case of CsPbX3 (X = Cl, Br, I). *Appl. Phys. Lett.* **2021**, *118*, No. 163901.

(14) Chen, P.; Liu, Y.; Zhang, Z.; Sun, Y.; Hou, J.; Zhao, G.; Zou, J.; Fang, Y.; Xu, J.; Dai, N. In situ growth of ultrasmall cesium lead bromine quantum dots in a mesoporous silica matrix and their application in flexible light-emitting diodes. *Nanoscale* **2019**, *11*, 16499−16507.

(15) Huang, L.; Dong, H.; Huo, N.; Zheng, Z.; Deng, H.-X.; Zhang, G.; Cheng, Y.; Li, J. Deep insights into interface engineering by buffer layer for efficient perovskite solar cells: a first-principles study. *Sci. China Mater.* **2020**, *63*, 1588−1596.

(16) Liu, X.; Tan, X.; Liu, Z.; Ye, H.; Sun, B.; Shi, T.; Tang, Z.; Liao, G. Boosting the efficiency of carbon-based planar CsPbBr3 perovskite solar cells by a modified multistep spin-coating technique and interface engineering. *Nano Energy* **2019**, *56*, 184−195.

(17) Xie, Q.; Wu, D.; Wang, X.; Li, Y.; Fang, F.; Wang, Z.; Ma, Y.; Su, M.; Peng, S.; Liu, H.; Wang, K.; Sun, X. W. Branched capping ligands improve the stability of cesium lead halide (CsPbBr3) perovskite quantum dots. *J. Mater. Chem. C* **2019**, *7*, 11251−11257.

(18) Acharyya, P.; Pal, P.; Samanta, P. K.; Sarkar, A.; Pati, S. K.; Biswas, K. Single pot synthesis of indirect band gap 2D CsPb2Br5 nanosheets from direct band gap 3D CsPbBr3 nanocrystals and the origin of their luminescence properties. *Nanoscale* **2019**, *11*, 4001−4007.

(19) Gan, Z.; Zheng, F.; Mao, W.; Zhou, C.; Chen, W.; Bach, U.; Tapping, P.; Kee, T. W.; Davis, J. A.; Jia, B.; Wen, X. The optical properties of Cs4PbBr6-CsPbBr3 perovskite composites. *Nanoscale* **2019**, *11*, 14676−14683.

(20) Yang, A.; Blancon, J. C.; Jiang, W.; Zhang, H.; Wong, J.; Yan, E.; Lin, Y. R.; Crochet, J.; Kanatzidis, M. G.; Jariwala, D.; Low, T.; Mohite, A. D.; Atwater, H. A. Giant Enhancement of Photoluminescence Emission in WS2-Two-Dimensional Perovskite Heterostructures. *Nano Lett.* **2019**, *19*, 4852−4860.

(21) Ghosh, D.; Walsh Atkins, P.; Islam, M. S.; Walker, A. B.; Eames, C. Good Vibrations: Locking of Octahedral Tilting in Mixed-Cation Iodide Perovskites for Solar Cells. *ACS Energy Lett.* **2017**, *2*, 2424−2429.

(22) Li, G.; Wang, H.; Zhu, Z.; Chang, Y.; Zhang, T.; Song, Z.; Jiang, Y. Shape and phase evolution from CsPbBr3 perovskite nanocubes to tetragonal CsPb2Br5 nanosheets with an indirect bandgap. *Chem. Commun.* **2016**, *52*, 11296−11299.

(23) Liang, T.; Liu, W.; Liu, X.; Li, Y.; Wu, W.; Fan, J. In Situ Phase-Transition Crystallization of All-Inorganic Water-Resistant Exciton-Radiative Heteroepitaxial CsPbBr3−CsPb2Br5 Core−Shell Perovskite Nanocrystals. *Chem. Mater.* **2021**, *33*, 4948−4959.

(24) Sun, C.; Gao, Z.; Deng, Y.; Liu, H.; Wang, L.; Su, S.; Li, P.; Li, H.; Zhang, Z.; Bi, W. Orange to Red, Emission-Tunable Mn-Doped Two-Dimensional Perovskites with High Luminescence and Stability. *ACS Appl. Mater. Interfaces* **2019**, *11*, 34109−34116.

(25) Su, Y.; Zeng, Q.; Chen, X.; Ye, W.; She, L.; Gao, X.; Ren, Z.; Li, X. Highly efficient CsPbBr3 perovskite nanocrystals induced by structure transformation between CsPbBr3 and Cs4PbBr6 phases. *J. Mater. Chem. C* **2019**, *7*, 7548−7553.

https://doi.org/10.1021/acsomega.2c01891
ACS Omega 2022, 7, 21800−21807